

Article

Superpixel-Based Classification Using K Distribution and Spatial Context for Polarimetric SAR Images

Qiao Xu, Qihao Chen, Shuai Yang and Xiuguo Liu *

Faculty of Information Engineering, China University of Geosciences (Wuhan), Wuhan 430074, China;
xu_qiao_cug@126.com (Q.X.); cugcqh@163.com (Q.C.); ys@2013.cug.edu.cn (S.Y.)

* Correspondence: liuxg318@hotmail.com; Tel.: +86-27-6788-3728; Fax: +86-27-6788-3809

Academic Editors: Heiko Balzter, Zhong Lu and Prasad S. Thenkabail

Received: 22 April 2016; Accepted: 21 July 2016; Published: 26 July 2016

Abstract: Classification techniques play an important role in the analysis of polarimetric synthetic aperture radar (PolSAR) images. PolSAR image classification is widely used in the fields of information extraction and scene interpretation or is performed as a preprocessing step for further applications. However, inherent speckle noise of PolSAR images hinders its application on further classification. A novel supervised superpixel-based classification method is proposed in this study to suppress the influence of speckle noise on PolSAR images for the purpose of obtaining accurate and consistent classification results. This method combines statistical information with spatial context information based on the stochastic expectation maximization (SEM) algorithm. First, a modified simple linear iterative clustering (SLIC) algorithm is utilized to generate superpixels as classification elements. Second, class posterior probabilities of superpixels are calculated by a K distribution in iterations of SEM. Then, a neighborhood function is defined to express the spatial relationship among adjacent superpixels quantitatively, and the class posterior probabilities are updated by this predefined neighborhood function in a probabilistic label relaxation (PLR) procedure. The final classification result is obtained by the maximum a posteriori decision rule. A simulated image, a spaceborne RADARSAT-2 image, and an airborne AIRSAR image are used to evaluate the proposed method, and the classification accuracy of our proposed method is 99.28%, 93.16% and 89.70%, respectively. The experimental results indicate that the proposed method obtains more accurate and consistent results than other methods.

Keywords: polarimetric synthetic aperture radar (PolSAR); image classification; superpixels; probabilistic label relaxation (PLR); K distribution

1. Introduction

1.1. Background

Synthetic aperture radar (SAR) is an active sensor that transmits and receives microwaves. Compared to optical remote sensing sensors, SAR has a day-or-night and all-weather imaging capability because of the penetrability of microwaves [1,2]. Polarimetric synthetic aperture radar (PolSAR) provides richer information than a single polarization channel as PolSAR transmits and receives electromagnetic waves in different states [3,4]. Given these advantages of PolSAR, it has been widely used for target detection and recognition, parameter inversion and land cover mapping [1–3,5].

With the launch of various spaceborne platforms, such as TerraSAR-X and RADARSAT-2, and the development of airborne platforms, such as AIRSAR and ESAR, an ever-increasing amount of PolSAR data becomes available. Therefore, developing automatic or semiautomatic interpretation systems for PolSAR images instead of manual interpretation is urgently necessary. In the past two decades, a number of methods have been developed. Among these methods, classification is one of the most

important techniques for PolSAR image interpretation to be used for information extraction and scene interpretation or performed as a preprocessing step for further applications. However, speckle noise appears in PolSAR images because of the coherent interference of waves reflected from elementary scatters. Such inherent speckle noise degrades the classification performance [6] and makes PolSAR image classification a challenging task. Many studies have focused on restraining this interference to improve classification accuracy. In summary, effective methods to solve this problem primarily include the following three aspects:

(1) Utilization of statistical information: Statistical properties of fully-developed speckle are widely used for the change detection, filtering and classification of PolSAR images [7–12]. In terms of classification, a specific data statistical distribution is generally adopted to model speckle noise. Many statistical models for PolSAR images are derived by physical or mathematical approaches. Among these models, the Gaussian-based Wishart distribution and non-Gaussian models are the most widely applied. However, these statistical models are complicated and have certain limitations. The Wishart distribution is mostly suitable for homogeneous areas, while non-Gaussian distributions effectively model heterogeneous areas. Thus, appropriate distribution and accurate parameter estimation methods are key issues in such methods.

(2) Utilization of spatial context information: The value of spatial context information has been verified in many studies. The spatial relationships between pixels help to reduce the interference of speckle noise and improve classification accuracy. An effective way to utilize spatial context information for PolSAR images is to combine it with statistical information.

(3) Object-oriented classification method: As the resolution of PolSAR images improves, coherent speckle noise becomes more complicated. The traditional pixel-based classification methods are significantly hindered by speckle noise, whereas the speckle noise could be effectively suppressed in the object-oriented classification method. However, image details suffer considerable losses when objects are used as processing elements. The appropriate method of the generation and utilization of objects is important for the object-oriented classification method.

1.2. Related Works

In the classification of PolSAR images, the analysis of physical scattering properties is widely studied. Typical classification methods have been proposed in such studies [3,13,14]. Moreover, many other new classification methods that utilize physical scattering properties have been developed in [2,15,16]. In this work, we focus on the three significant topics in PolSAR image classification: statistical classification, contextual classification and object-oriented classification.

(1) Statistical classification for PolSAR images: Multi-look PolSAR data are represented by a coherency matrix and satisfy the Gaussian-based complex Wishart distribution in homogenous areas [9]. Thus, different statistical distance measures, such as maximum likelihood distance [10], revised Wishart distance [11] and Wishart test distance [12], are derived for PolSAR image classification; these methods have achieved significant results in homogeneous areas. However, the Wishart distribution has the limitation of characterizing heterogeneous areas because of the absence of modeling texture components. Lee et al. [17] utilized the gamma distribution to model texture components and developed the well-known K distribution based on the product model. Doulgeris et al. [18] utilized the finite mixture model (FMM) based on the K distribution to classify PolSAR images. Beaulieu et al. [19] used the likelihood merging criteria derived from the K distribution to obtain accurate segments of PolSAR images. Moreover, other heterogeneous models, such as G^0 , KummerU and the L distribution, have been proposed by means of the scalar product model. Several scholars have adopted these models in PolSAR image classification [20–22] and demonstrated satisfactory results in modeling heterogeneous areas. However, these statistical models are complicated, and finding an accurate and stable estimation of its distribution parameters is still a challenge.

(2) Contextual classification for PolSAR images: The Markov random field (MRF) has been used to describe spatial context information together with statistical information in PolSAR image classification.

Wu et al. [23] incorporated the Wishart distribution with MRF for PolSAR image classification. Akbari et al. [6] proposed an unsupervised classification method based on the K distribution and MRF. An adaptive MRF with spatial variant FMM was proposed in [24]. All of these works demonstrate that MRF can effectively improve classification accuracy. In addition, the probabilistic label relaxation (PLR) model is a rather simple and effective method to incorporate spatial context information; this model employs the probability of joint events between a given pixel and its neighbors [25]. The PLR method has been applied to optical image classification [25,26]. Moreover, Reigber et al. [27] utilized the PLR to express spatial context information instead of MRF in their classification experiment and showed that PLR could remove isolated pixels in classification results caused by speckle noise or misclassification. In addition, Mohammed et al. [28] proposed a new neighborhood-supported function to describe the spatial relationships between pixels.

(3) Object-oriented classification for PolSAR images: Among the developed classification methods, pixel-based classification methods have obtained fair results. However, several drawbacks in the traditional pixel-based classification still exist due to inherent speckle noise [23,27,29,30]. By contrast, object-oriented classification offers a promising scheme. Li et al. [29] utilized support vector machine (SVM) for PolSAR image classification based on the objects generated by the region growing technique. Benz and Pointier [30] proposed an object-based fuzzy classification method for PolSAR images using the eCognition software. He et al. [31] utilized the SVM classifier to obtain PolSAR image classification results based on a novel over-segmentation method. In recent studies, superpixels have been incorporated into object-oriented land cover classification for PolSAR images. Liu et al. [32] used the normalized cuts algorithm to generate superpixels and conducted classification experiments based on superpixels. Feng et al. [33] and Song et al. [34] used superpixels generated by the simple linear iterative clustering (SLIC) algorithm as their classification elements. These works demonstrate the feasibility of superpixels.

1.3. The Proposed Approach

Compared to the aforementioned methods, two improvements are included in the proposed method. One is the comprehensive utilization of the K distribution and spatial context information described by the PLR model; the other is the utilization of superpixels as processing elements. Specifically, when a specific PolSAR data statistical distribution is applied to classification, accurate parameter estimation is essential to obtain fair results. Given that the stochastic expectation maximization (SEM) algorithm is an efficient iteration estimation algorithm for complicated models and is likely to avoid local extremes in the log-likelihood function during iterations [6], the SEM algorithm has recently been employed for PolSAR image classification [6,24,35]. In the SEM algorithm, the classification result is iteratively refined by the maximum a posteriori (MAP) decision rule until the convergence criterion is met, and the statistical distributions of each class are estimated according to the previous classified image. Thus, a posteriori probabilities are significant to the SEM algorithm. The K distribution is adopted in the present study to ensure the accuracy and stability of probability calculation.

Considering that MRF has a complicated likelihood function and is computationally expensive to optimize, the present study utilized the PLR model to describe spatial context information. In the conventional PLR procedure, a maximum likelihood classification is performed, and class probabilities can be easily calculated through the iteration of SEM. Then, PLR is utilized to alter the a posteriori probabilities in SEM using a predefined neighborhood function. In the end, a novel contextual SEM clustering method is proposed in the present work.

Among the many superpixel-generating algorithms, the SLIC algorithm is designed to generate a set of compact superpixels efficiently [36] and has been successfully applied for PolSAR images [33,34,37]. Thus, a modified SLIC algorithm is proposed for PolSAR images in the present study. Moreover, a novel supervised superpixel-based SEM clustering framework using the K distribution and spatial context information for PolSAR images is presented. First, the modified SLIC algorithm is used to

generate superpixels as subsequent processing elements. Second, the initial parameters of the K distribution for each class are estimated according to the training samples, then the K distribution is utilized to calculate the class posterior probabilities of superpixels in the expectation step, and the posterior probabilities are altered by a neighborhood function among adjacent superpixels in PLR iterations. Afterward, the image is randomly labeled in the stochastic step based on the previous probabilities. Then, the K distribution is updated according to the classified image in the maximization step. The SEM algorithm iterates through the aforementioned three steps until a certain convergence criterion is met; the final classification result is obtained by the MAP decision rule. The performance of the proposed method is presented and analyzed using one simulated image and two real-world PolSAR images.

The remainder of this paper is organized as follows: The proposed classification method is explained in Section 2. The employed PolSAR images and the experimental and evaluation results are reported in Section 3. The discussion of the results is presented in Section 4. The conclusions are given in Section 5.

2. Methodology

The proposed method consists of three main parts: (1) superpixel generation in PolSAR images by the SLIC algorithm; (2) utilization of the PLR model; and (3) clustering process of the SEM algorithm. The details of these three parts are explained in the subsequent subsections with a flowchart in Figure 1 to illustrate the structure of our method.

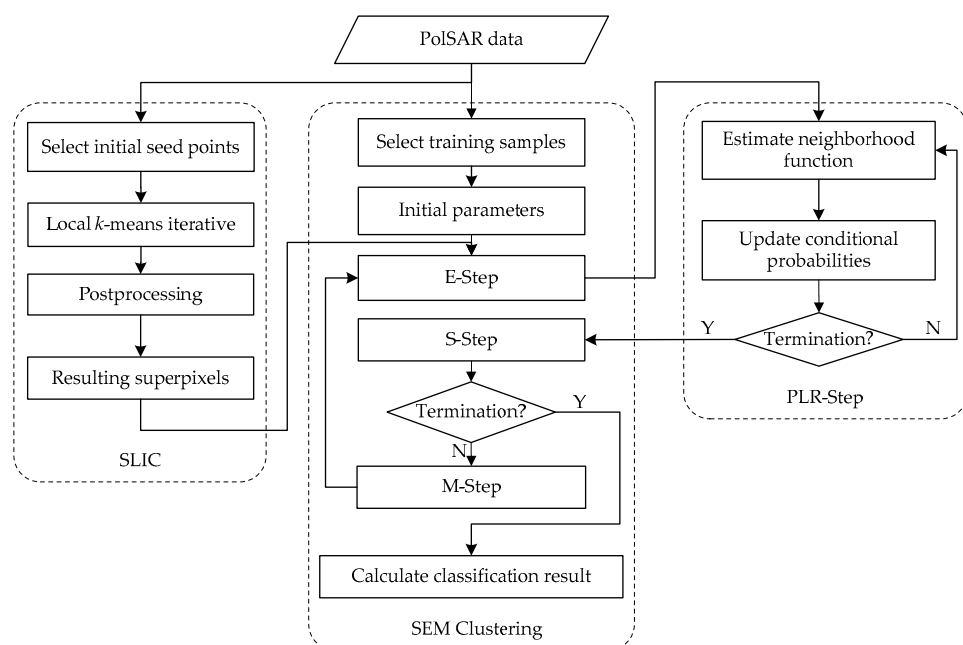


Figure 1. Overview of the proposed contextual SEM algorithm for PolSAR data classification. SLIC, simple linear iterative clustering.

2.1. Superpixel Generation in PolSAR Images

A superpixel is a spatially-continuous collection of pixels with similar characteristics, which adheres well to image boundaries. Thus, superpixels are generally utilized as a preprocessing step to increase the speed and improve the quality of the results. In the field of image classification, pixels within one superpixel are assumed to be of the same class, and superpixels are utilized as classification elements to suppress the influence of speckle noise. For PolSAR images, coherent speckle noise is an important factor reducing image classification accuracy. In recent years, superpixel-based classification methods have achieved fair results in PolSAR image. The SLIC algorithm is able to

generate compact, approximately homogeneous superpixels with high computational efficiency and has been successfully utilized in optical and PolSAR images [33,34,37]. We modify the SLIC algorithm to control the superpixel generation in PolSAR images, and the main steps are as follows:

(1) Select the initial center seed points: pixels are sampled as seed points at equal intervals according to step length S in the Pauli RGB gradient image. Then, the seeds are moved to locations corresponding to the lowest gradient position in a 3×3 neighborhood. These seeds are taken as initial superpixel centers.

(2) Local k -means iterative clustering: The distance between the superpixel center and each pixel in the $2S \times 2S$ region around the superpixel center is calculated. Then, each pixel is assigned to the nearest superpixel. After all of the centers are processed, each superpixel center is updated. This step is repeated until convergence or until the maximum number of iterations is reached. Then, superpixels are generated, and the expected spatial extent of a superpixel is a region of an approximate size of $S \times S$.

(3) Post-processing: The regions whose sizes are less than a specific threshold are merged with the nearest neighbors according to the distance measure. Then, the final superpixels of PolSAR images are achieved.

As described in the aforementioned steps, the distance measure between pixels and the superpixel centers is the key issue of the SLIC algorithm. In the optical image, the distance is defined by weighting spectral distance and spatial distance, which are clearly unsuitable for PolSAR images. Therefore, several scholars have utilized different statistical distances derived from the Wishart distribution to replace spectral distance [33,34,37]. However, the statistical distance is unstable when the superpixels are small in size, which could affect the accuracy of superpixels.

Polarimetric decomposition parameters are important signatures of ground objects for PolSAR images. In particular, the three components of Pauli decomposition have clear physical meanings and represent odd-bounce scattering and double-bounce scattering from corners with relative orientations of 0° and 45° , respectively. The Pauli RGB image is the standard display mode of PolSAR images. Based on the aforementioned consideration, the Pauli decomposition feature is adopted to replace the spectral feature, and the Pauli distance and spatial distance are combined into a single measurement. Assuming that the center locations of the i -th and j -th superpixel are (x_i, y_i) and (x_j, y_j) , their Pauli decomposition feature vectors are (Pa_i, Pb_i, Pc_i) and (Pa_j, Pb_j, Pc_j) respectively. The spatial distance and Pauli distance measurement is defined as follows:

$$\begin{aligned} d_s &= \sqrt{(x_i - x_j)^2 + (y_i - y_j)^2} \\ d_p &= \sqrt{(Pa_i - Pa_j)^2 + (Pb_i - Pb_j)^2 + (Pc_i - Pc_j)^2} \end{aligned} \quad (1)$$

The combined distance measurement is defined as follows:

$$d = \sqrt{\frac{d_p}{maxd_p} + \beta \left(\frac{d_s}{S} \right)^2} \quad (2)$$

where $maxd_p$ is the maximum value of the Pauli distance of the last iteration, which is utilized to normalize the Pauli distance, and β is a weight parameter. When β is small, the generated superpixels have less regular sizes and shapes. When β is large, the spatial proximity is significant, and the generated superpixels become compact. Drawing on the experience of Song et al. [34] and our own experiment experience, we set $\beta = 1$ for the remainder of the study to obtain a reasonable result.

2.2. Superpixel-Based PLR Model

The distance measurement expressed as Equations (1) and (2) is used to generate superpixels. Actually, the adjacent superpixels are dependent. Ground targets are continuously distributed, and the category of each superpixel is affected by neighborhood information in the real world. The PLR model is an iterative labeling algorithm considering neighborhood information, which is based on the

assumption that the adjacent pixels are spatially related, rather than statistically independent. Based on this idea, our study takes superpixels as classification elements, and the superpixel-based PLR model is proposed to incorporate spatial context information among adjacent superpixels. If the neighborhood superpixels are classified into a class with high probability, then the current superpixel is more likely to belong to that same class. Figure 2 shows the difference of the definition of neighborhood systems between the pixel-based and superpixel-based PLR model.

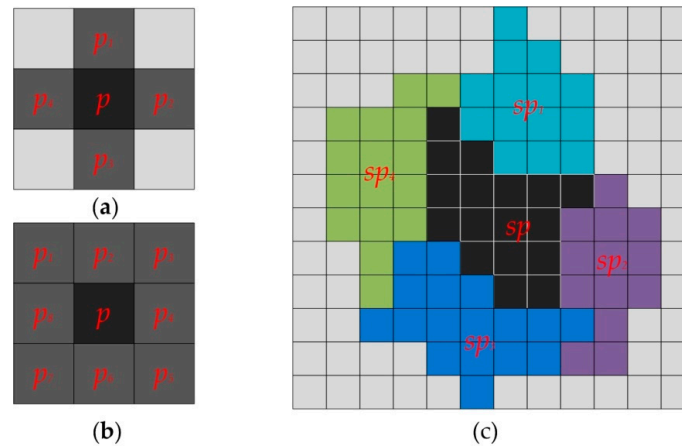


Figure 2. Definition of the neighborhood systems with the pixel and the superpixel: (a) pixel-based four-neighborhood system of center pixel p ; (b) pixel-based eight-neighborhood system of center pixel p and (c) superpixel-based neighborhood system of center superpixel sp .

The compatibility coefficient $p_{sn}(\omega_i|\omega_j)$ describes the probability of a superpixel sp belonging to class ω_i when the neighborhood superpixel sp_n is of class ω_j . The compatibility coefficient generally derives from the geometric distribution of the actual ground targets. However, this information is unknown. In this case, single value ρ is utilized to approximate the compatibility coefficients as follows:

$$p_{sn}(\omega_i|\omega_j) = \begin{cases} \rho & ; \omega_i = \omega_j \\ 1 - \rho & ; \omega_i \neq \omega_j \end{cases} \quad (3)$$

The value of ρ quantifies the probability of convergence between equal classes, and a consistent result can be derived from a high value of ρ . Then, the contribution of the neighborhood superpixel sp_n with class label ω_j to superpixel sp belonging to class ω_i can be written with joint probability as follows:

$$p_{sn}(\omega_i, \omega_j) = p_{sn}(\omega_i|\omega_j) \times p_n(\omega_j) \quad (4)$$

where $p_n(\omega_j)$ is the prior probability. Given that an arbitrary superpixel sp consisting of N neighborhood superpixels and M possible class assignments are possible, a neighborhood function is defined as follows:

$$q_s(\omega_i) = \sum_{n=1}^N d_n \sum_{j=1}^M p_{sn}(\omega_i|\omega_j) \times p_n(\omega_j) \quad (5)$$

$$d_n = \frac{NP_n}{NP_s}$$

where d_n is the neighborhood weight related by the ratio of the number of pixels NP_n and NP_s in current superpixels and $q_s(\omega_i)$ represents the contribution of all neighborhood superpixels to the superpixel with the current class label. Combining the spatial neighborhood contribution calculated by Equation (5) with the local observation calculated by the K distribution, the class probability of a superpixel sp is updated as follows:

$$p_s^{t+1}(\omega_i) = \frac{p_s^t(\omega_i) q_s^t(\omega_i)}{\sum_j p_s^t(\omega_j) q_s^t(\omega_j)} \quad (6)$$

where t is the iteration index in the PLR. Class probabilities are altered in each iteration and approach convergence after multiple iterations. Such convergence can be measured by the change of conditional probabilities and is defined as follows:

$$CP^t = \sum_{s=1}^N ||p_s^t - p_s^{t-1}|| \quad (7)$$

When the value is less than 1%, the iteration stops.

2.3. SEM Clustering Utilizing the K Distribution

The aforementioned PLR model is implemented as a step of SEM clustering to take statistical information and spatial context information into account for PolSAR image classification. This section presents the SEM clustering utilization K distribution and PLR model, which consists of two parts: the PolSAR K distribution and the new process of SEM clustering.

2.3.1. PolSAR K Distribution

In a reciprocal medium, the scattering matrix can be transformed into a scattering vector using the basis set of Pauli spin matrices. The scattering vector is expressed as follows:

$$\mathbf{k} = \frac{1}{\sqrt{2}} \begin{bmatrix} S_{hh} + S_{vv} & S_{hh} - S_{vv} & 2S_{hv} \end{bmatrix}^T \quad (8)$$

where the factor $\sqrt{2}$ is used to conserve the total scattered power, S_{ij} is the complex element of the scattering matrix, HV is the vertically-polarized transmitting antenna and horizontally-polarized receiving antenna and the superscript T is the transpose operator. The n -look coherency matrix is written as follows:

$$T = \langle \mathbf{k} \mathbf{k}^H \rangle = \frac{1}{L} \sum_{i=1}^L \mathbf{k}(i) \mathbf{k}(i)^H \quad (9)$$

where $\langle \cdot \rangle$ denotes the spatial average operator, L is the number of looks and the superscript H indicates the complex conjugate transposition. Speckle is assumed to be fully developed and to have a zero-mean circular complex Gaussian process. Thus, the coherency matrix T follows the Wishart distribution denoted as $W(L, \Sigma)$. The probability density function (PDF) is expressed as follows:

$$p(T|\Sigma) = \frac{\det(T) \exp\left\{-L\text{tr}\left(\Sigma^{-1}T\right)\right\}}{Q(L) \det(\Sigma)^L} \quad (10)$$

with:

$$Q(L) = \frac{\pi^3 \Gamma(L) \Gamma(L-1) \Gamma(L-2)}{L^{3L}} \quad (11)$$

where $\Sigma = E[\mathbf{k} \mathbf{k}^H]$ is the expectation of the coherency matrix, $\Gamma(\cdot)$ denotes the gamma function and $\text{tr}(\cdot)$ and $\det(\cdot)$ denote the trace and determinant of the matrix, respectively. The Wishart distribution is suitable for homogeneous areas, such as water bodies, farmlands and roads. It is, however, less effective in modeling heterogeneous areas with rich texture information. The gamma distribution is generally utilized to model texture component σ and has been proven effective [19]. Its PDF is expressed as follows:

$$p(\sigma|\alpha) = \frac{\sigma^{\alpha-1} \alpha^\alpha}{\Gamma(\alpha)} \exp[-\alpha\sigma] \quad (12)$$

where $\alpha > 0$ is the shape parameter and $E[\sigma] = 1$, $\text{var}[\sigma] = 1/\alpha$. Assuming that the texture component is polarization independent, the Wishart distribution and the gamma distribution are utilized to model coherent speckle components and texture components, respectively. Then, the K distribution can be

derived from the product model for the multi-look coherency matrix, denoted by $KW(L, \alpha, \Sigma)$. Its PDF is expressed as follows:

$$p(T|\Sigma, L, \alpha) = \frac{2|T|^{L-3} (L\alpha)^{(\alpha+3L)/2}}{\pi^3 \Gamma(L) \Gamma(L-1) \Gamma(L-2) \Gamma(\alpha)} \cdot \frac{K_{\alpha-3L} \left(2\sqrt{\text{tr}(\Sigma^{-1}T)} L\alpha \right)}{\det(\Sigma)^L \text{tr}(\Sigma^{-1}T)^{(3L-\alpha)/2}} \quad (13)$$

where $K_v(\cdot)$ is the modified Bessel function of the second kind with order v . The K distribution is parameterized by the shape parameter α , the number of looks L and the scale matrix Σ . 1D $\text{tr}(\Sigma^{-1}T)$ is used to transform the complex matrix data into a scalar to display the K distribution of the coherency matrix data visually. The corresponding PDF is evaluated as intensity $KW(Ld, \alpha, d)$. Similarly, the Wishart distribution after transformation is equivalent to the 1D gamma distribution [18]. Figure 3 shows the K distribution with different shape parameters and the corresponding gamma distribution. As we can see, a high value of α indicates low texture. When $\alpha \rightarrow \infty$, the texture variable tends to be constant, and the K distribution asymptotically converges to the Wishart distribution. Therefore, the flexible K distribution captures real data variations compared to the Wishart distribution in a better way.

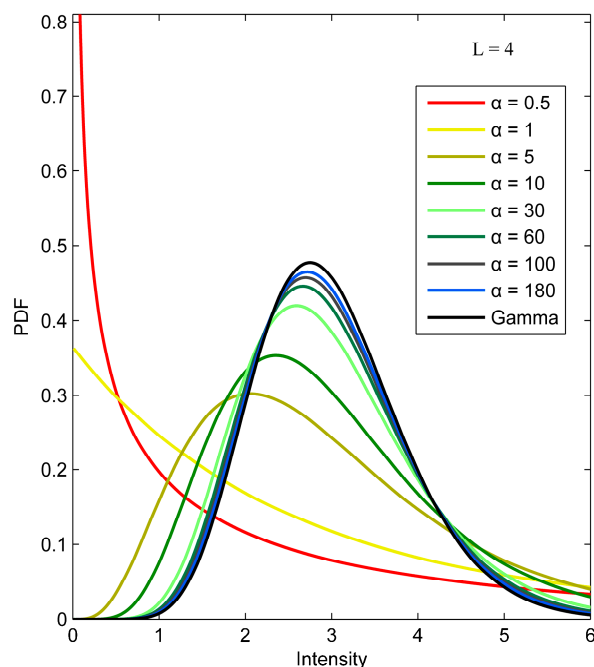


Figure 3. Theoretical intensity curves of the K distribution with different shape parameters and the Wishart distribution after $\text{tr}(\Sigma^{-1}T)$ transformation.

The correct form of the K distribution is decided by the appropriate estimation of the parameters. In this distribution model, the scale matrix Σ is the expectation of the coherency matrix, and the estimated value $\hat{\Sigma}$ can be calculated by the sample average as follows:

$$\hat{\Sigma} = \langle T \rangle \quad (14)$$

Given that a spatial correlation exists between different polarimetric channels, then the number of looks L in Equation (13) should be replaced by the equivalent number of looks (ENL). For PolSAR data, the ENL and shape parameter have been traditionally estimated separately for each polarimetric channel and then averaged, as in [38]. However, this method ignores the polarimetric information

and is unreliable, whereas the direct use of the coherency matrix or covariance matrix obtains good results. Consequently, the method of matrix log-cumulants (MoMLC) [39] is adopted to estimate ENL and shape parameter α in our method. MoMLC has been widely used and proven to be an effective estimation technique with respect to the PolSAR product model. The following equation is utilized to estimate ENL [39]:

$$\langle \ln |T| \rangle - \ln |\langle T \rangle| - \sum_{i=0}^2 \Psi^{(i)} (\hat{L} - i) + 3\ln \hat{L} = 0 \quad (15)$$

where $\Psi^{(i)}(\cdot)$ denotes a polygamma function. Then, the overdetermined system of MoMLC equations is utilized to estimate the shape parameter by the weighted least square method, which is explained in detail in [39].

2.3.2. SEM Clustering Processing

Image classification can be regarded as dividing an image into separate finite classes; the FMM is utilized to describe the statistical distribution of the samples within mixture classes [40]. The FMM assumes that each observation datum is composed of different class components, and each class component is weighted by the normalized probabilities. When a superpixel is taken as an observation element, coherency matrix T_{sp} , which is averaged by pixels in each superpixel, is used to represent the superpixel. The PDF of T_{sp} is written as follows:

$$p(T_{sp}; \Theta) = \sum_{i=1}^J \mu_i p_i(T_{sp}; \theta_i) \quad (16)$$

$$T_{sp} = \langle T_s \rangle$$

where T_s is the coherency matrix of pixels in a superpixel, μ_i is the prior probability of class i in a total of J classes and satisfies $\sum_{i=1}^J \mu_i = 1$, θ_i is the parameter vector of the K distribution for the i -th class, $p_i(\cdot | \theta_i)$ is the PDF for the i -th class and $\Theta = (\mu_1, \mu_2, \dots, \mu_J, \theta_1, \theta_2, \dots, \theta_J)$ is the parameter vector of FMM. The log-likelihood function expressed in Equation (17) is maximized to obtain the best image partition with J classes.

$$LL(\Theta) = \sum_{sp \in S} (\log(p(T_{sp}; \Theta))) = \sum_{sp \in S} \left(\log \left(\sum_{i=1}^J \mu_i p_i(T_{sp}; \theta_i) \right) \right) \quad (17)$$

However, the parameter vector and class labels are unknown and must be estimated from the observations, which makes it an incomplete data problem. Since the SEM algorithm is an effective parameter estimation method, especially for incomplete data, and is insensitive to the number of training samples [26], it is employed to solve the problem. Given that the category of each superpixel is affected by the surrounding superpixels, the spatial context information between adjacent superpixels should be considered. Thus, a contextual SEM algorithm is developed for PolSAR image classification.

The proposed contextual SEM classifier consists of two processing stages, namely the SEM stage and the PLR stage. The K distribution is employed in the SEM stage to obtain accurate probabilities of class membership. These probabilities are altered in the PLR stage by the neighborhood function. The method is described in detail as follows:

Initialization: Training samples are selected for each class. The initial parameter θ_i of each class is calculated, and the initial prior probability μ_i for the i -th class is set as $1/J$.

Expectation (E) step: For each superpixel, the probabilities of class membership are calculated utilizing the K distribution, and the posterior probabilities τ_{sp}^k are updated as follows:

$$\tau_{sp}^k (T_{sp} | \omega_i; \Theta^k) = \frac{\mu_i^k p_i(T_{sp}; \theta_i^k)}{\sum_{j=1}^J \mu_j^k p_j(T_{sp}; \theta_j^k)} \quad (18)$$

PLR step: The probabilities of class membership are altered based on the neighborhood function, as described in Equation (6), until the convergence criterion is met.

Stochastic (S) step: Each pixel is randomly labeled as different classes according to the current estimated posterior probability from the PLR step.

Maximization (M) step: The prior probability is updated using the relative frequency assigned to each class, and the shape parameter and ENL of the K distribution are re-estimated.

The contextual SEM algorithm iterates through these four steps until it converges or reaches the maximum number of iterations. The total category change rate is used as the termination criterion as follows:

$$CC^k = \frac{1}{2} \left\{ \sum_{i=1}^J \sum_{j=1, i \neq j}^J p_{i \rightarrow j}^k \right\} / Num \quad (19)$$

where $p_{i \rightarrow j}^k$ represents the number of pixels changed from class i to class j in iteration k and Num is the number of total pixels. If the total change rate is less than 1%, then the algorithm is terminated, and each superpixel is assigned to the most likely class according to the posterior probability. In summary, the proposed method is presented in Algorithm 1.

Algorithm 1: Superpixel-based SEM clustering utilizing the K distribution.

```

1: INPUT: PolSAR image, training samples, maximum iterations of SEM MAX.
2: OUTPUT: classification image Label.
3: Generate superpixels of PolSAR image by SLIC method by Equations (1) and (2).
4: Compute initial  $K$  distribution parameters  $\theta(n)$  by the MoMLC method by Equation (15) with
   training samples.
5: Do
6:    $k = k + 1$ 
7:   for each superpixel  $SP(i) \in SP$  do
8:     Compute posterior probabilities of each class  $\tau_{sp}^k$  by Equations (13) and (18).
9:   end for
10:  for each superpixel  $SP(i) \in SP$  do
11:    Update  $\tau_{sp}^k$  following Equations (4)–(6)
12:  end for
13:  for each superpixel  $SP(i) \in SP$  do
14:    Compute Label( $i$ ) by randomly labeling according to  $\tau_{sp}^k$ .
15:  end for
16:  if ( $k \geq 2$ ) do compute termination criterion  $CC^k$  following Equation (19).
17:  if ( $CC^k < 1\%$ ) goto Step 19, and compute final classification results.
18: While ( $k \leq MAX$ )
19: for each superpixel  $SP(i) \in SP$  do
20:   Compute classification result Label( $i$ ) by the MAP decision rule according to  $\tau_{sp}^k$ .
21: end for
```

3. Experiment and Results

The ultimate goal of our research is to develop a PolSAR image classification method that can suppress coherent speckle noise to obtain an accurate and consistent classification result. In this section, one simulated dataset and two different real-world PolSAR datasets were used to evaluate the proposed method. In our experiments, different classification methods were used for comparison. The overall accuracy (OA) and kappa coefficient were calculated to evaluate the performance. The section is divided into two subsections to describe the experimental datasets and to show the experimental details of the simulated PolSAR image, RADARSAT-2 image and AIRSAR image.

3.1. Description of the Experimental Datasets

The first dataset is a simulated PolSAR image generated by the method described in [9], which is 800 pixels \times 800 pixels in size and composed of eight different classes, including road, water body, grass-land, different types of crops, bush land, forest and urban areas. Among these classes, water body was generated by the Wishart distributed matrix data, and the other classes were generated by the K distribution matrix data. The initial coherency matrix and distribution parameters were estimated from the real dataset to simulate classes with properties of real-world images. The Pauli decomposition composite image is shown in Figure 4a, and the manual classification map of the simulated image is shown in Figure 4b with the areas of training samples marked by boxes. The intensity curves of each class after $tr(\Sigma^{-1}T)$ transformation are shown in Figure 5, and it can be seen that the eight classes are simulated with different shape parameters, which ensures that various degrees of texture are included in the simulated image.

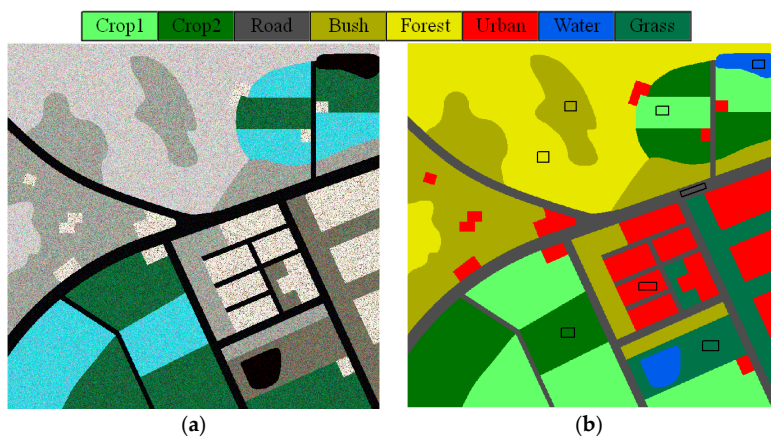


Figure 4. Simulated PolSAR image as the first dataset used in the experiment: (a) Pauli color-coded image and (b) the manual classification map of the simulated image. Boxes in (b) are the areas of the training samples for the simulated image.

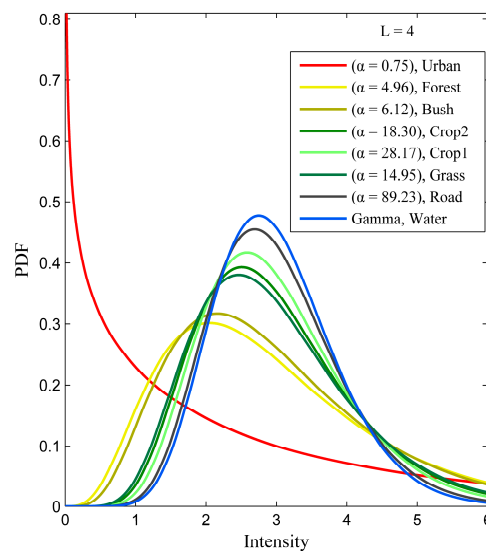


Figure 5. Intensity curves for each simulated class datum after $tr(\Sigma^{-1}T)$ transformation.

The second dataset is obtained from a subset of a C-band RADARSAT-2 Fine-Quad-Mode fully-PolSAR image acquired over northern Flevoland, The Netherlands, on 2 April 2008. The major

land cover classes include homogeneous areas, such as water body and farmlands, and heterogeneous areas, such as forest and urban areas. The four-look processed experimental image with a size of 780 pixels \times 700 pixels is shown in Figure 6a. Manual classification according to the corresponding optical image was used as the ground truth map, as shown in Figure 6b. The areas of training samples for the RADARSAT-2 image are marked by boxes in Figure 6b.

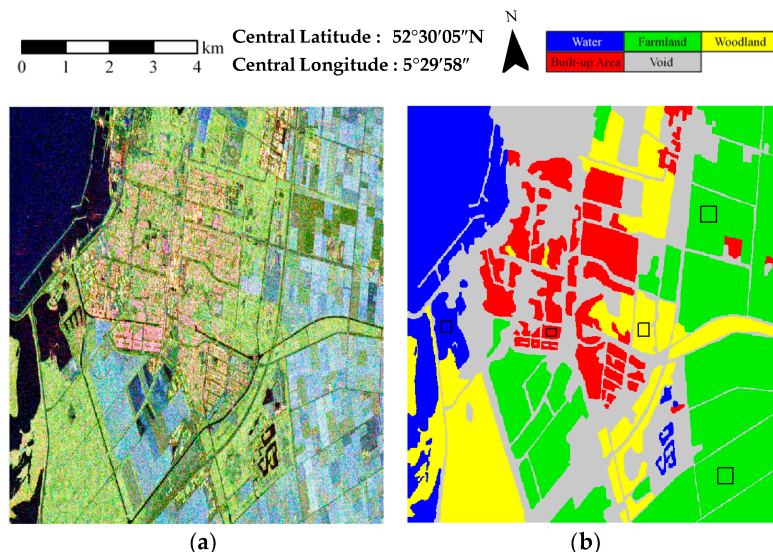


Figure 6. C-band, multi-look PolSAR image of Flevoland of RADARSAT-2 as the second dataset used in the experiment: (a) Pauli color-coded image and (b) the ground truth map of (a). Boxes in (b) are the areas of training samples for the RADARSAT-2 data.

The third dataset is obtained from a section of the four-look processed PolSAR image of an agricultural area over Flevoland, The Netherlands, from an airborne AIRSAR L-band in August 1989. The experimental image with the size of 380 pixels \times 424 pixels is shown in Figure 7a. The ground truth map is taken from [23,32] and is shown in Figure 7b. According to the ground truth map, seven classes of crops and one class of bare soil are present in the experimental image. The areas of training samples for the AIRSAR image are marked by boxes in Figure 7b.

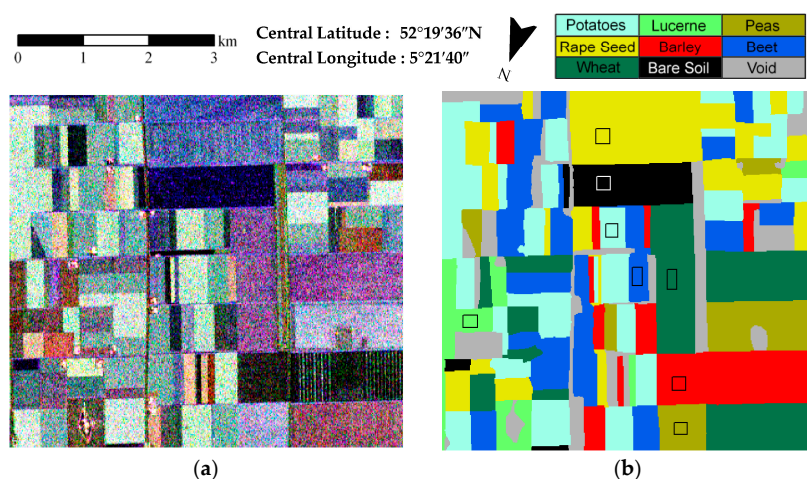


Figure 7. L-band, multi-look PolSAR image of Flevoland of AIRSAR as the third dataset used in the experiment: (a) Pauli color-coded image and (b) the ground truth map of (a). Boxes in (b) are the areas of training samples for the AIRSAR data.

3.2. Evaluation and Comparison

The proposed algorithms were implemented using the C++ language. The Boost library was used to calculate the parameters of the K distribution and class probabilities. A desktop computer with a 32-bit Windows XP operating system, a quad-core Intel Core i3-2120 CPU, 3.3 GHz and 4 GB memory was utilized for the experiment.

Classification experiments with the simulated image were performed using different methods, namely (a) SEM classification utilizing the K distribution based on pixels (KSEM); (b) KSEM classification based on superpixels (SP-KSEM); (c) KSEM classification combined with PLR (KSEM-PLR) based on pixels and (d) KSEM-PLR classification based on superpixels (SP-KSEM-PLR), to verify the improvement of classification accuracy by introducing superpixels and spatial context information to the SEM algorithm. The SLIC superpixel map (4 pixels \times 4 pixels in size) of the simulated image is shown in Figure 8a. Figure 8b shows the local boundary details in the upper right corner of the superpixel map. Figure 8c–f shows the classification results of the four methods. The OA and kappa coefficients are shown in Table 1.

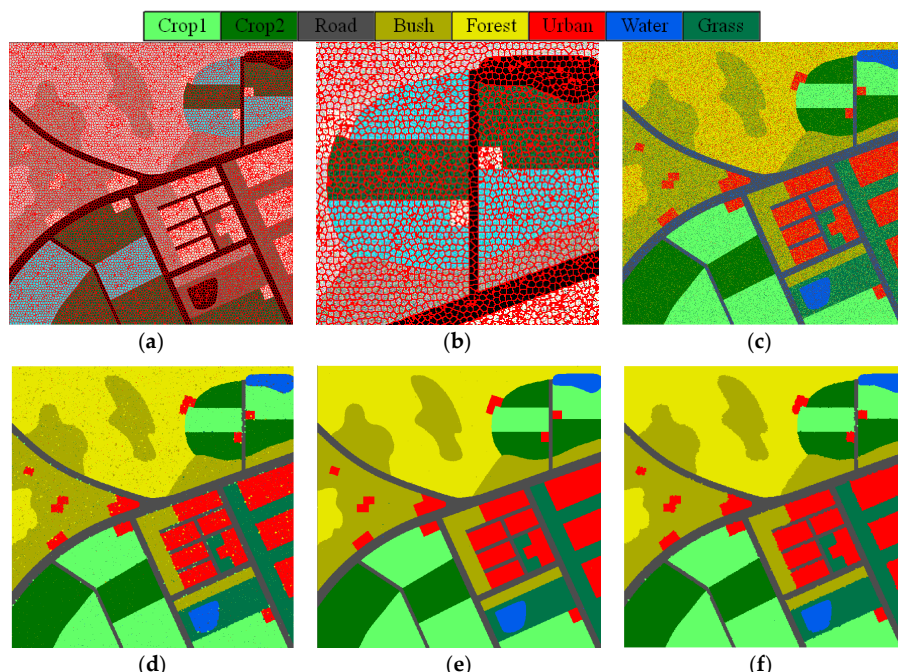


Figure 8. Classification results of the simulated image with different methods: (a) superpixel map; (b) enlarged view of the upper right corner of the superpixel map; (c) SEM classification utilizing the K distribution (KSEM); (d) superpixel (SP)-KSEM; (e) KSEM-PLR; and (f) SP-KSEM-PLR.

Table 1. Classification accuracy measures of the simulated image.

Method	KSEM	SP-KSEM	KSEM-PLR	SP-KSEM-PLR
OA	78.74	97.33	99.84	99.28
Kappa	0.751	0.968	0.998	0.991

As shown in Figure 8 and Table 1, the pixel-based KSEM-PLR method obtained the best classification results. The pixel-based KSEM method had the lowest classification accuracy, and the salt-and-pepper phenomenon occurred in its classification result, particularly for the forest and urban areas. Compared to the pixel-based KSEM method, the SP-KSEM method obtained more consistent results, and its OA was improved to 97.33%. However, misclassifications still occurred for forest and urban areas. For the SP-KSEM-PLR method, the classification result was more consistent,

and the OA increased by approximately 2% compared to the SP-KSEM method. However, partial class boundaries of the SP-KSEM-PLR method were inaccurate, and the OA was slightly lower than that of the pixel-based KSEM-PLR method. In summary, experiments on the simulated PolSAR image demonstrate the effectiveness of using superpixels and spatial context information. Employing superpixels suppresses the interference of speckle noise, and the spatial context information helps to remove isolated superpixels in the classification result.

The superpixel-based classification method using the Wishart distribution (SP-WSEM-PLR) was supplemented for the RADARSAT-2 and AIRSAR images to validate the performance of the proposed method further. The pixels categorized as void were ignored. The sizes of the superpixels of the RADARSAT-2 and AIRSAR images were 7 pixels \times 7 pixels and 4 pixels \times 4 pixels, respectively. The superpixel map and classification results of the different methods of RADARSAT-2 and AIRSAR images are shown in Figures 9 and 10, respectively. The OA and kappa coefficients are presented in Tables 2 and 3, respectively.

For the RADARSAT-2 image, the pixel-based method KSEM had the worst classification accuracy according to Figure 9 and Table 2. When spatial context information is added to the pixel-based KSEM method (KSEM-PLR), the classification accuracy increased from 69.99% to 85.07%, and the result became more consistent. Compared to the pixel-based KSEM method, the SP-KSEM method improved classification accuracy from 69.99% to 84.12%. Thus, the superpixel-based method contributes to suppressing speckle noise. However, several isolated superpixels existed in the built-up areas. As shown in Table 2, the proposed SP-KSEM-PLR method obtained the highest classification accuracy, reaching 93.16%; in particular, the performance of the built-up areas exhibited a significant improvement. For the SP-WSEM-PLR method, the classification accuracy of the built-up areas increased by 10.11%, and the OA increased by 2.52%. Thus, the K distribution is effective for modeling the built-up areas.

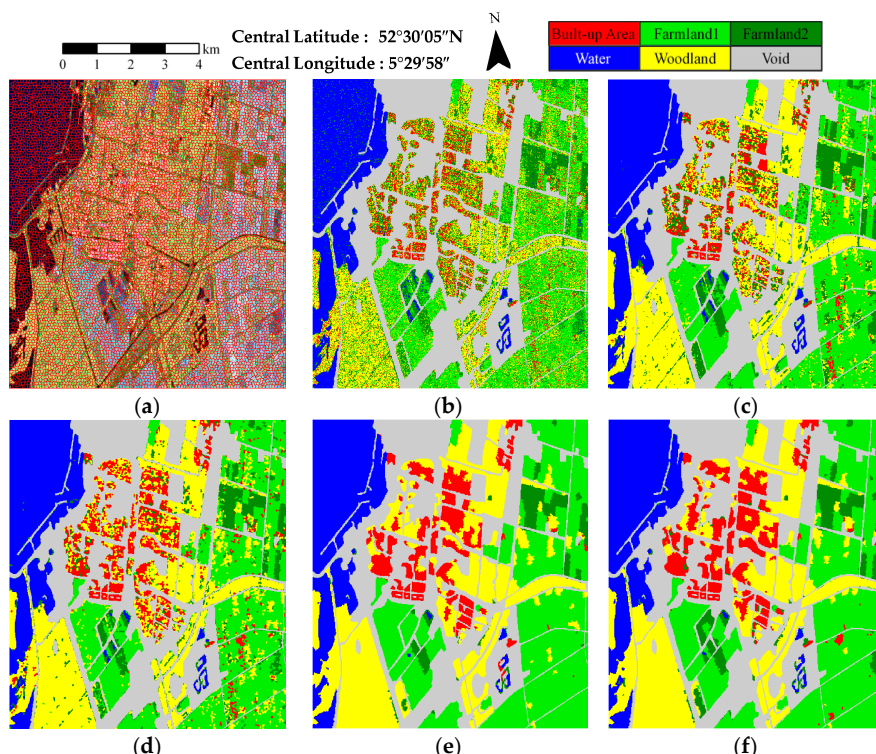


Figure 9. Classification results of the RADARSAT-2 image with different methods: (a) superpixel map; (b) KSEM; (c) KSEM-PLR; (d) SP-KSEM; (e) SP-WSEM-PLR (Wishart distribution SEM (WSEM)); and (f) SP-KSEM-PLR.

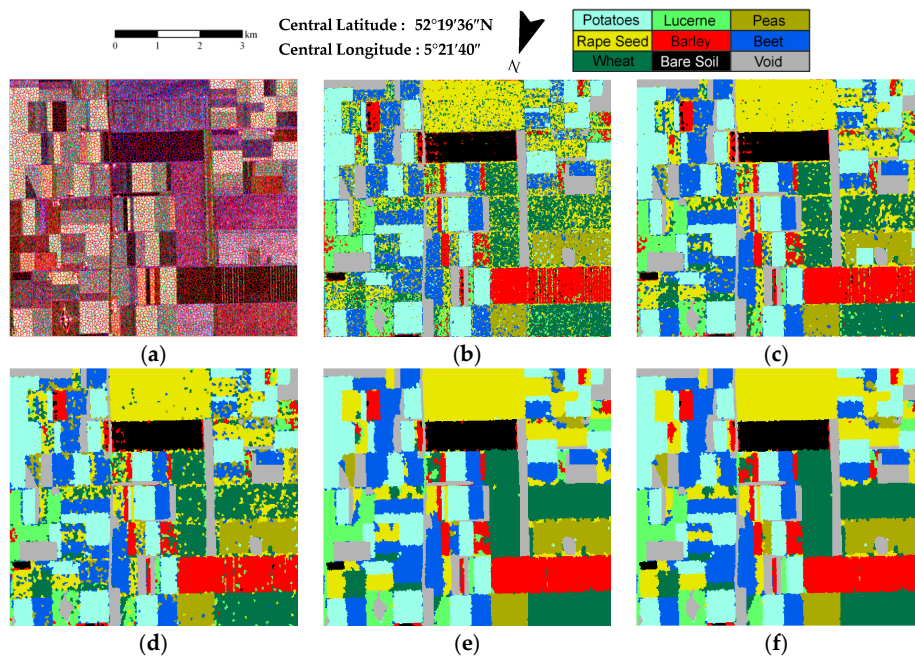


Figure 10. Classification results of the AIRSAR image with different methods: (a) superpixel map; (b) KSEM; (c) KSEM-PLR; (d) SP-KSEM; (e) SP-WSEM-PLR; and (f) SP-KSEM-PLR.

Table 2. Classification accuracy measures of the RADARSAT-2 image.

Method	Water	Farmland	Woodland	Built-up Area	OA	Kappa
KSEM	94.22	76.29	60.18	35.05	69.99	0.566
KSEM-PLR	98.46	89.18	88.06	50.69	85.07	0.785
SP-KSEM	96.67	85.02	90.47	55.10	84.13	0.775
SP-WSEM-PLR	97.45	93.54	98.15	61.43	90.65	0.867
SP-KSEM-PLR	95.61	97.03	97.65	71.54	93.16	0.902

Table 3. Classification accuracy measures of the AIRSAR image.

Method	KSEM	KSEM-PLR	SP-KSEM	SP-WSEM-PLR	SP-KSEM-PLR
Potatoes	90.93	94.00	94.31	95.86	95.83
Lucerne	76.63	83.88	83.04	93.74	94.51
Peas	65.93	64.91	78.62	82.20	88.64
Rape Seed	66.69	78.77	76.23	85.26	87.23
Barely	73.04	78.83	75.49	80.75	83.77
Beet	70.67	81.64	77.70	89.81	90.15
Wheat	66.41	76.73	78.52	87.42	87.28
Bare Soil	89.56	91.14	86.98	89.39	90.07
OA	74.52	81.85	81.55	88.45	89.70
Kappa	0.700	0.786	0.782	0.864	0.878

For the AIRSAR image, the proposed SP-KSEM-PLR method obtained the highest OA and consistent classification results. The contrast between Figure 10b,d and Figure 10c,f certifies that superpixels help to suppress speckle noise in the PolSAR images. The classification results shown in Figure 10b–d,f demonstrate the validity of the spatial context information incorporated into the classification. Given that the study areas are homogeneous, the classification accuracy of SP-WSEM-PLR is quite close to that of SP-KSEM-PLR, which shows that the *K* distribution is also able to describe homogeneous areas effectively.

4. Discussion

4.1. Main Features of the Proposed Method

The superpixel-based SEM classification method using the K distribution and spatial context information is proposed, which was successfully applied to the simulated and real-world PolSAR images. The main advantage of the proposed approach is the generation of accurate and consistent classification results.

In the related studies, many other methods use the Wishart distribution to represent the scattering vector statistics for the PolSAR image classification [9–12,14,27,40]. Given the absence of modeling texture components, the Wishart distribution is unsuitable for heterogeneous areas, and the K distribution is used in the proposed approach instead. On the other hand, several experiments demonstrated better classification results when using spatial context information among adjacent pixels [6,23–27,30]. The MRF model is generally utilized to describe the spatial context information [6,23,24]; however, it is computationally expensive to optimize due to the complicated likelihood function. Thus, our method adopts the PLR model to express the spatial context information. In summary, the main feature of our method is the comprehensive utilization of the K distribution and the PLR model.

Most of the previous works utilized pixels as the processing elements for PolSAR image classification, which is likely to produce a typically inconsistent salt-and-pepper classification result [29,30]. To address this problem, object-oriented classification is a promising scheme. Superpixels have been adopted in object-oriented land cover classification. Liu et al. [32], Feng et al. [33] and Song et al. [34] utilized superpixels as classification elements, and the validity of superpixels was proven by their experiments. The present study used the modified SLIC algorithm to generate superpixels as classification elements, and spatial context information among the adjacent superpixels is effectively incorporated in this approach. Thus, another feature of our method is the utilization of superpixels. This approach is capable of suppressing speckle noise and obtaining consistent classification results compared to the traditional pixel-based classification.

4.2. Sensitivity Analysis of the Parameters

4.2.1. Size of Superpixels

According to the classification experiments with simulated and real-world PolSAR images, the size of superpixels affects classification accuracy. In particular, more surface detail information is lost when the size of superpixels is sufficiently large; this information loss results in an inaccurate class boundary. When the size of superpixels is small, suppressing speckle noise becomes difficult, and the salt-and-pepper phenomenon is likely to appear in its classification result. Therefore, choosing the appropriate size of superpixels is a key issue. An additional experiment was conducted to analyze the effect of the size of superpixels on classification accuracy. In the process of generating superpixels, different sizes of superpixels were set. Then, the proposed SP-KSEM-PLR method was utilized in the classification experiment. The changes of the OA and kappa coefficients with different sizes of the superpixels for the simulated data, RADARSAT-2 and AIRSAR images are shown in Figures 11 and 12, respectively.

As shown in Figures 11 and 12, the size of superpixels has a significant effect on the proposed superpixel-based classification method. For the simulated image, the OA decreases when the size of superpixels increases from 1 pixel \times 1 pixel to 10 pixels \times 10 pixels. Thus, using superpixels for the simulated data is unnecessary. The simulated image is known to satisfy the statistical distribution strictly and cannot describe the complicated ground class distribution. The pixel-based KSEM-PLR is able to eliminate speckle noise interference by incorporating spatial context information. On this basis, superpixel-based classification leads to the loss of surface details and consequently decreases the classification accuracy of the simulated image. Therefore, the pixel-based KSEM-PLR method obtained higher OA than the SP-KSEM-PLR method in the simulated data experiments.

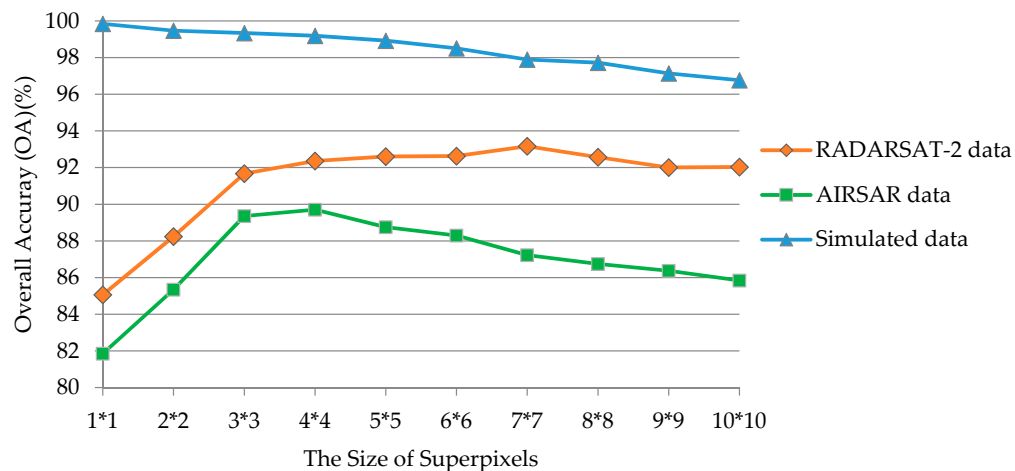


Figure 11. OA obtained by applying SP-KSEM-PLR to the simulated, RADARSAT-2 and AIRSAR images using different sizes of superpixels.

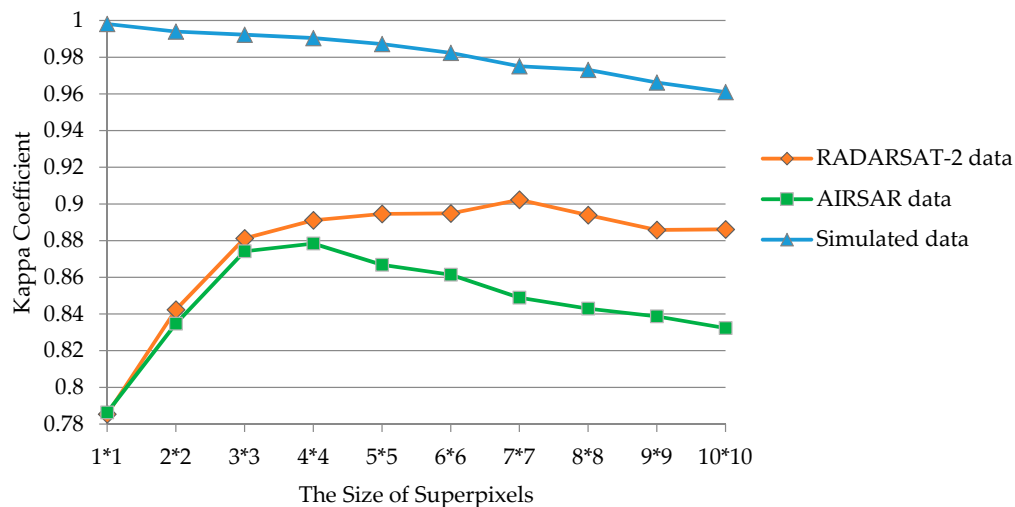


Figure 12. Kappa coefficients obtained by applying SP-KSEM-PLR to the simulated, RADARSAT-2 and AIRSAR images using different sizes of superpixels.

For the RADARSAT-2 image, OA improves when the size of superpixels increases from 3 pixels \times 3 pixels to 7 pixels \times 7 pixels and decreases when the size of superpixels exceeds 7 pixels \times 7 pixels. Thus, superpixels with a size of 7 pixels \times 7 pixels were generated as classification elements for the RADARSAT-2 image classification experiment. Similarly, when the size of superpixels is 4 pixels \times 4 pixels, the classification of the AIRSAR image obtained the highest OA. Thus, superpixels were generated with a size of 4 pixels \times 4 pixels for the AIRSAR image.

The selection of the appropriate size of superpixels could be regarded as an optimal segmentation scale selection problem for object-oriented classification, which is quite complicated. For the proposed method, the appropriate size of superpixels depends on the complexity of the PolSAR images, and the cross-validation method could be helpful to set the size of superpixels based on the training samples. The land cover types and speckle noise of the RADARSAT-2 image are more complicated than that of the AIRSAR image. Thus, a larger size of superpixels is needed for the RADARSAT-2 image. In summary, if the scene of the PolSAR images is simple, then a small size of superpixels is preferred. By contrast, the large size of superpixels is essential to obtain an accurate result for the scenes of images that are complicated.

4.2.2. Iteration Times of the PLR Step

According to the previous presented classification experiments, spatial context information has improved the classification performance for the three different images. The number of iterations of the PLR model affects the utilization of spatial context information. The PLR step in the process of the SP-KSEM-PLR method for the RADARSAT-2 image was iterated for different times to analyze the performance of combining spatial context information with the SEM framework; the final classification results are shown in Figure 13, and the change of OA and kappa coefficients with different PLR step iteration times is shown in Figures 14 and 15, respectively.

Figures 13–15 show the impacts of introducing spatial context information to the SEM framework for the RADARSAT-2 image. In Figure 13a, the classification result appears relatively noisy because spatial context information was not fully utilized. As the number of iterations on the neighborhood function increases, the consistency and accuracy of the classification result improved (Figure 13b–d), and the class boundaries and point targets, such as individual buildings, were preserved well. As shown in Figure 14, when the number of iterations increased to 15, OA was improved to 92.30%; the PLR step approached convergence; and the spatial context information was fully utilized. Similar to the RADARSAT-2 image, optimal results were obtained for the simulated and AIRSAR images when the PLR step terminated. As the number of iterations of the PLR step increases, the classification results became more accurate and consistent.

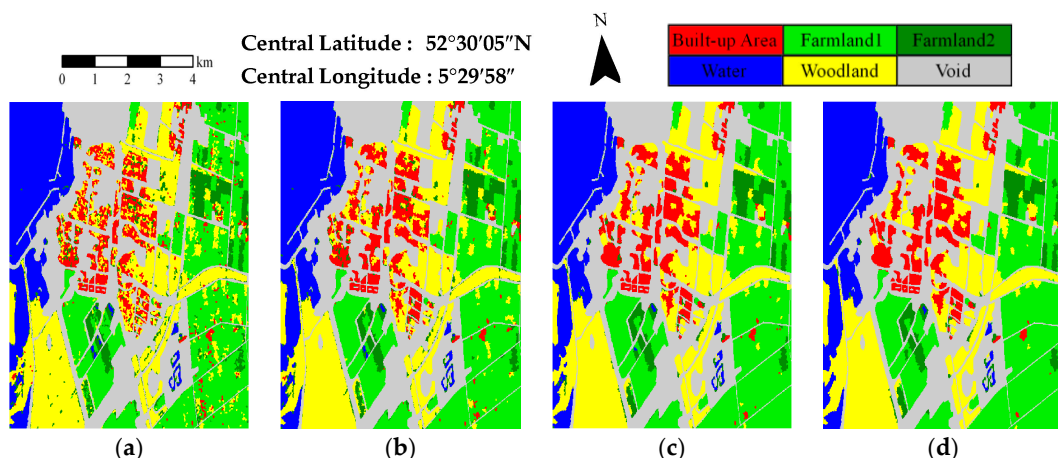


Figure 13. Classification results of the RADARSAT-2 image with different PLR step iteration times: (a) one time; (b) five times; (c) 15 times; and (d) 45 times.

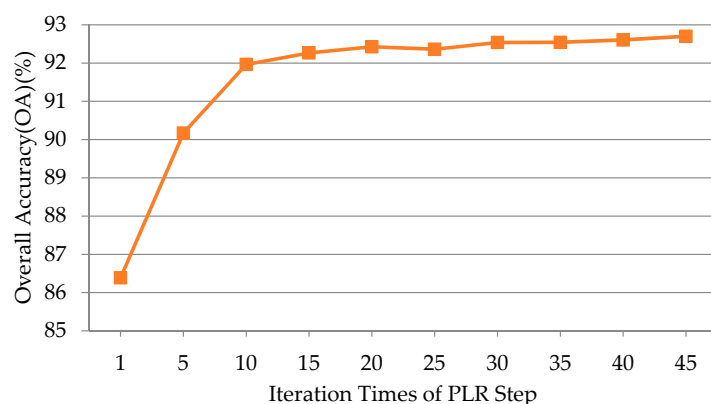


Figure 14. OA of applying SP-KSEM-PLR to the RADARSAT-2 image with different PLR step iteration times.

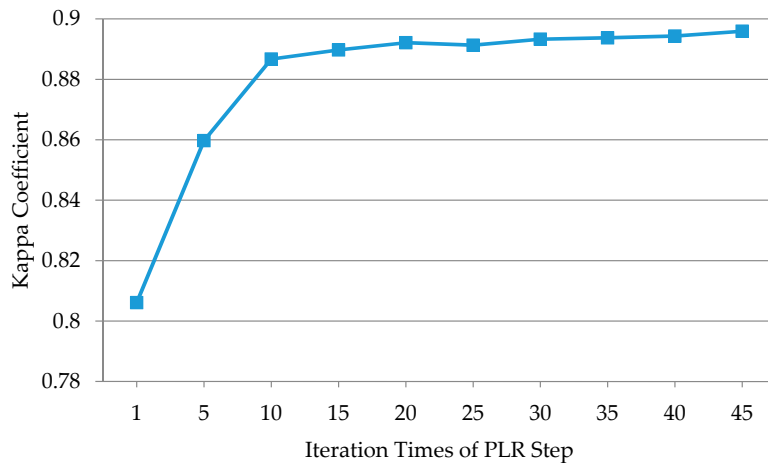


Figure 15. Kappa coefficients of applying SP-KSEM-PLR to the RADARSAT-2 image with different PLR step iteration times.

4.3. Accuracies, Errors and Uncertainties

In the experiments, ground truth data were used for the validation of our proposed method. The OA and kappa coefficient were used to evaluate the accuracy performance of the classification; these two measures are widely accepted in remote sensing image classification. The comparative trials demonstrated that the classification accuracy was improved with our proposed method.

Considering the previous experiments, several factors affect the classification accuracy of the proposed method. The initial parameters of K distribution depend on the training samples. When the two types of the training samples are quite similar, the form of K distribution for the two classes could be similar when the SEM terminates. This similarity causes misclassifications between the two classes. In addition, if the values of shape parameters of two classes are indeed close, these two classes will be hard to distinguish, and misclassification may appear. The estimation accuracy of the shape parameter is another factor that causes classification errors. During the process of estimating the shape parameter of the K distribution, the squared Mahalanobis distance (explained in detail in [39]) should be minimized. Achieving the accurate solution of the equation is sometimes difficult, and consequently, an approximate solution is adopted as an alternative. Therefore, errors can occur when the form of the K distribution is inaccurate. The future development of this approach should include the strategy for the selection of training samples and the accurate parameter estimation method for the K distribution.

The performance of the proposed method is demonstrated using a simulated image and real-world RADARSAT-2 and AIRSAR images; these images mainly cover water body, farmlands, forest and built-up areas. Thus, the classification results may vary for other different scenarios. The proposed method is mainly designed for such major classification categories; the experimental results demonstrated that the proposed method performed well. However, in-depth experiments and analyses for other subclasses, such as collapsed buildings, coniferous forest and broadleaf forest, have not been conducted in the present study. Thus, the applicability of the proposed method for PolSAR image subclassification remains uncertain.

5. Conclusions

Coherent speckle noise is an inherent property of polarimetric Synthetic Aperture Radar (PolSAR) images; this noise makes PolSAR image classification a challenging task. In this study, a novel supervised superpixel-based stochastic expectation maximization (SEM) clustering method for PolSAR images is developed by combining the K distribution with spatial context information. This method aims to obtain accurate and consistent classification results for PolSAR images. The main improvements are as follows: First, superpixels generated by the modified simple linear iterative clustering (SLIC)

algorithm are utilized as classification elements to suppress the influence of speckle noise. Second, the superpixel-based spatial context information described by the probabilistic label relaxation (PLR) model is incorporated to alter the posterior probabilities, which are calculated by the K distribution in the expectation step of the SEM clustering. This strategy controls the isolated superpixels in the classification results that are caused by misclassification or speckle noise.

Comparative experiments using a simulated image, a spaceborne RADARSAT-2 image and an airborne AIRSAR image were conducted to verify the validity and applicability of the proposed method. The proposed approach achieved the highest accuracy for real-world datasets (93.16% on RADARSAT-2 image and 89.70% on AIRSAR image), which is much improved in contrast to other methods. For the simulated image, superpixels are non-essential to the classification. The overall accuracy (OA) of the proposed method is 0.56% lower than that of the pixel-based KSEM-PLR method because of the information loss of surface details caused by superpixels. In conclusion, accurate and consistent classification results can be obtained by the proposed method for PolSAR images.

However, further improvements are required. The strategy of selecting training samples, setting the size of superpixels and the parameter estimation method could be optimized. In addition, polarimetric decomposition parameters are important signatures for PolSAR images. Future efforts should be devoted to improving the performance of PolSAR image classification by incorporating polarimetric decomposition parameters in the proposed method.

Acknowledgments: This work is supported in part by the National Natural Science Foundation of China under Grant Nos. 41471355 and 41301477. We also thank Qi Chen, Xiaoli Xing and Linlin Li for their support during the entire course of this study.

Author Contributions: Qiao Xu drafted the manuscript and was responsible for the research design and experiment. Qihao Chen and Shuai Yang reviewed the manuscript and were responsible for the analysis. Xiuguo Liu supervised the research and contributed to the editing and review of the manuscript.

Conflicts of Interest: The authors declare no conflict of interest.

References

1. Wei, J.; Zhang, J.; Huang, G.; Zhao, Z. On the use of Cross-Correlation between volume scattering and helix scattering from polarimetric SAR data for the improvement of ship detection. *Remote Sens.* **2016**, *8*, 74. [[CrossRef](#)]
2. Ressel, R.; Singha, S. Comparing near coincident space borne C and X band fully polarimetric SAR data for arctic sea ice classification. *Remote Sens.* **2016**, *8*, 198. [[CrossRef](#)]
3. Cloude, S.R.; Pottier, E. An entropy based classification scheme for land applications of polarimetric SAR. *IEEE Trans. Geosci. Remote Sens.* **1997**, *35*, 68–78. [[CrossRef](#)]
4. Touzi, R.; Boerner, W.M.; Lee, J.S.; Lueneburg, E. A review of polarimetry in the context of synthetic aperture radar: Concepts and information extraction. *Can. J. Remote Sens.* **2004**, *30*, 380–407. [[CrossRef](#)]
5. Huang, X.; Wang, J.; Shang, J. An integrated surface parameter inversion scheme over agricultural fields at early growing stages by means of C-band polarimetric RADARSAT-2 imagery. *IEEE Trans. Geosci. Remote Sens.* **2016**, *54*, 2510–2528. [[CrossRef](#)]
6. Akbari, V.; Doulgeris, A.P.; Moser, G.; Eltoft, T.; Anfinsen, S.N.; Serpico, S.B. A textural–contextual model for unsupervised segmentation of multipolarization synthetic aperture radar images. *IEEE Trans. Geosci. Remote Sens.* **2013**, *51*, 2442–2453. [[CrossRef](#)]
7. Conradsen, K.; Nielsen, A.A.; Schou, J.; Skriver, H. A test statistic in the complex Wishart distribution and its application to change detection in polarimetric SAR data. *IEEE Trans. Geosci. Remote Sens.* **2003**, *41*, 4–19. [[CrossRef](#)]
8. Lee, J.-S.; Ainsworth, T.L.; Wang, Y.; Chen, K.S. Polarimetric SAR speckle filtering and the extended sigma filter. *IEEE Trans. Geosci. Remote Sens.* **2015**, *53*, 1150–1160. [[CrossRef](#)]
9. Du, L.J.; Lee, J.-S. Classification of multi-look polarimetric SAR imagery based on complex Wishart distribution. *Int. J. Remote Sens.* **1994**, *15*, 2299–2311.

10. Lee, J.-S.; Grunes, M.R.; Ainsworth, T.L.; Du, L.; Schuler, D.L.; Cloude, S.R. Unsupervised classification using polarimetric decomposition and the complex Wishart classifier. *IEEE Trans. Geosci. Remote Sens.* **1999**, *37*, 2249–2258.
11. Alonso-Gonzalez, A.; Lopez-Martinez, C.; Salembier, P. Filtering and segmentation of polarimetric SAR data based on binary partition Trees. *IEEE Trans. Geosci. Remote Sens.* **2012**, *50*, 593–605. [[CrossRef](#)]
12. Kersten, P.R.; Lee, J.-S.; Ainsworth, T.L. Unsupervised classification of polarimetric synthetic aperture Radar images using fuzzy clustering and EM clustering. *IEEE Trans. Geosci. Remote Sens.* **2005**, *43*, 519–527. [[CrossRef](#)]
13. Van Zyl, J.J. Unsupervised classification of scattering behavior using radar polarimetry data. *IEEE Trans. Geosci. Remote Sens.* **1989**, *27*, 36–45. [[CrossRef](#)]
14. Ferro-Famil, L.; Pottier, E.; Lee, J. Unsupervised classification of multifrequency and fully polarimetric SAR images based on the H/A/Alpha-Wishart classifier. *IEEE Trans. Geosci. Remote Sens.* **2001**, *39*, 2332–2342. [[CrossRef](#)]
15. Morandeira, N.; Grings, F.; Facchinetto, C.; Kandus, P. Mapping plant functional types in floodplain wetlands: An analysis of C-band polarimetric SAR Data from RADARSAT-2. *Remote Sens.* **2016**, *8*, 174. [[CrossRef](#)]
16. Jafari, M.; Maghsoudi, Y.; Zanjani, M.J.V. A new method for land cover characterization and classification of polarimetric SAR data using polarimetric signatures. *IEEE J. Sel. Top. Appl. Earth Obs. Remote Sens.* **2015**, *8*, 3595–3607. [[CrossRef](#)]
17. Lee, J.-S.; Schuler, D.L.; Lang, R.H.; Ranson, K.J. K-distribution for multi-look processed polarimetric SAR imagery. In Proceedings of the International Geoscience and Remote Sensing Symposium IGARSS ‘94. Surface and Atmospheric Remote Sensing: Technologies, Data Analysis and Interpretation, Pasadena, CA, USA, 8–12 August 1994; pp. 2179–2181.
18. Doulgeris, A.P.; Anfinsen, S.N.; Eltoft, T. Classification with a non-Gaussian model for PolSAR data. *IEEE Trans. Geosci. Remote Sens.* **2008**, *46*, 2999–3009. [[CrossRef](#)]
19. Beaulieu, J.M.; Touzi, R. Segmentation of textured polarimetric SAR scenes by likelihood approximation. *IEEE Trans. Geosci. Remote Sens.* **2004**, *42*, 2063–2072. [[CrossRef](#)]
20. Horta, M.M.; Mascarenhas, N.D.A.; Frery, A.C.; Levada, A.L.M. Clustering of fully polarimetric SAR data using finite Gp^0 mixture model and SEM Algorithm. In Proceedings of the 15th International Conference on Systems, Signals and Image Processing, Bratislava, Slovakia, 25–28 June 2008; pp. 81–84.
21. Tison, C.; Nicolas, J.M.; Tupin, F.; Maitre, H. A new statistical model for Markovian classification of urban areas in high-resolution SAR images. *IEEE Trans. Geosci. Remote Sens.* **2004**, *42*, 2046–2057. [[CrossRef](#)]
22. Song, W.; Li, M.; Zhang, P.; Wu, Y.; Jia, L.; An, L. The WGI distribution for multilook polarimetric SAR data and its application. *IEEE Geosci. Remote Sens. Lett.* **2015**, *12*, 2056–2060. [[CrossRef](#)]
23. Wu, Y.; Ji, K.; Yu, W.; Su, Y. Region-based classification of polarimetric SAR images using Wishart MRF. *IEEE Geosci. Remote Sens. Lett.* **2008**, *5*, 668–672. [[CrossRef](#)]
24. Niu, X.; Ban, Y. An adaptive contextual SEM algorithm for urban land cover mapping using multitemporal high-resolution polarimetric SAR data. *IEEE J. Sel. Top. Appl. Earth Obs. Remote Sens.* **2012**, *5*, 1129–1139. [[CrossRef](#)]
25. Khodadadzadeh, M.; Ghassemian, H. A novel contextual classification of hyperspectral data using probabilistic label relaxation process. In Proceedings of the 19th Iranian Conference on Electrical Engineering (ICEE), Tehran, Iran, 17–19 May 2011; pp. 1–5.
26. Richards, J.A.; Jia, X. A Dempster-Shafer relaxation approach to context classification. *IEEE Trans. Geosci. Remote Sens.* **2007**, *45*, 1422–1431. [[CrossRef](#)]
27. Reigber, A.; Jaeger, M.; Neumann, M.; Ferro-Famil, L. Classifying polarimetric SAR data by combining expectation methods with spatial context. *Int. J. Remote Sens.* **2010**, *31*, 727–744. [[CrossRef](#)]
28. Dabboor, M.; Shokr, M. A new Likelihood Ratio for supervised classification of fully polarimetric SAR data: An application for sea ice type mapping. *ISPRS J. Photogramm. Remote Sens.* **2013**, *84*, 1–11. [[CrossRef](#)]
29. Li, H.T.; Gu, H.Y.; Han, Y.S.; Yang, J.H. Object-oriented classification of polarimetric SAR imagery based on statistical region merging and support vector machine. In Proceedings of the International Workshop on Earth Observation and Remote Sensing Applications, Beijing, China, 30 June–2 July 2008; pp. 147–152.
30. Benz, U.; Pottier, E. Object based analysis of polarimetric SAR data in alpha-entropy-anisotropy decomposition using fuzzy classification by eCognition. In Proceedings of the IEEE International Geoscience and Remote Sensing Symposium, Sydney, Australia, 9–13 July 2001; pp. 1427–1429.

31. He, C.; Deng, J.; Xu, L.; Li, S.; Duan, M.; Liao, M. A novel over-segmentation method for polarimetric SAR images classification. In Proceedings of the IEEE International Geoscience and Remote Sensing Symposium, Munich, Germany, 22–27 July 2012; pp. 4299–4302.
32. Liu, B.; Hu, H.; Wang, H.; Wang, K.; Liu, X.; Yu, W. Superpixel-based classification with an adaptive number of classes for polarimetric SAR images. *IEEE Trans. Geosci. Remote Sens.* **2013**, *51*, 907–924. [[CrossRef](#)]
33. Feng, J.; Cao, Z.; Pi, Y. Polarimetric contextual classification of PolSAR Images using sparse representation and superpixels. *Remote Sens.* **2014**, *6*, 7158–7181. [[CrossRef](#)]
34. Song, H.; Yang, W.; Bai, Y.; Xu, X. Unsupervised classification of polarimetric SAR imagery using large-scale spectral clustering with spatial constraints. *Int. J. Remote Sens.* **2015**, *36*, 2816–2830. [[CrossRef](#)]
35. Niu, X.; Ban, Y. A novel contextual classification algorithm for multitemporal polarimetric SAR data. *IEEE Geosci. Remote Sens. Lett.* **2014**, *11*, 681–685.
36. Achanta, R.; Shaji, A.; Smith, K.; Lucchi, A.; Fua, P.; Süstrunk, S. SLIC Superpixels compared to state-of-the-art superpixel methods. *IEEE Trans. Pattern Anal. Mach. Intell.* **2012**, *34*, 2274–2282. [[CrossRef](#)] [[PubMed](#)]
37. Qin, F.; Guo, J.; Lang, F. Superpixel Segmentation for polarimetric SAR imagery using local iterative clustering. *IEEE Geosci. Remote Sens. Lett.* **2015**, *12*, 13–17.
38. Frery, A.C.; Correia, A.H.; Freitas, C.D.C. Classifying multifrequency fully polarimetric imagery with multiple sources of statistical evidence and contextual information. *IEEE Trans. Geosci. Remote Sens.* **2007**, *45*, 3098–3109. [[CrossRef](#)]
39. Anfinsen, S.N.; Eltoft, T. Application of the matrix-variate Mellin transform to analysis of polarimetric radar images. *IEEE Trans. Geosci. Remote Sens.* **2011**, *49*, 2281–2295. [[CrossRef](#)]
40. Gao, W.; Yang, J.; Ma, W. Land cover classification for polarimetric SAR Images based on mixture models. *Remote Sens.* **2014**, *6*, 3770–3790. [[CrossRef](#)]



© 2016 by the authors; licensee MDPI, Basel, Switzerland. This article is an open access article distributed under the terms and conditions of the Creative Commons Attribution (CC-BY) license (<http://creativecommons.org/licenses/by/4.0/>).